Catalysis Science & Technology

ROYAL SOCIETY OF CHEMISTRY

PAPER

View Article Online
View Journal | View Issue

Check for updates

Cite this: *Catal. Sci. Technol.*, 2025, **15**, 4713

On the enhanced photocatalytic activity of N-doped carbon dots†

Hector Daniel Almeida Gonzalez, [a] Gabriel Rafael Guerrero Porras, [b] Hervé Vezin, [c] Lisandra Morales Alvarez, [d] Angel Luis Corcho Valdés, [d] L. Julieth Bravo Martínez, [e] Alicia M. Díaz-García, [b] David González-Martínez, [f] Jose M. Moran-Mirabal, [fg] Clarissa Murru, [h] Johnny Deschamps, [i] Claudia Iriarte-Mesa, [jk] Qixiang Jiang, [l] Freddy Kleitz, [j] Luis Felipe Desdin-Garcia *[d] and Manuel Antuch *[dm]

Carbon nanostructures (dots) have emerged as a novel and sustainable alternative for the photocatalytic degradation of water pollutants. This work presents the synthesis of multidoped carbon nanomaterials (CNs) using a microwave-assisted method. Overall, four types of carbon nanostructures were obtained: (i) nitrogen-doped CNs (N-CDs), (ii) nitrogen and sulfur co-doped CNs (N,S-CNs), (iii) nitrogen and phosphorus co-doped CNs (N,P-CNs), and (iv) nitrogen, sulfur, and phosphorus multi-doped CNs (N,S,P-CNs). The characterization of these nanoparticles was performed *via* Fourier-transform infrared spectroscopy (FTIR) and X-ray photoelectron spectroscopy (XPS), enabling the identification of stretching modes corresponding to C=O, C–N, and N–H functional groups. Additionally, UV-vis and fluorescence spectroscopies allowed the detection of n–π* and π–π* absorption bands at ~325 and 400 nm, along with light emission at 438 nm. High-resolution transmission electron microscopy (TEM) characterization confirmed structural and morphological differences between the nanomaterials, which exhibited sizes ranging from 1 to 100 nm, depending on the chemical composition of the starting precursors. Finally, the photocatalytic activity of the CNs towards the degradation of toluidine blue was assessed, considering the effects of morphology, composition, and both catalyst and dye concentration on photodegradation. Such a catalytic process followed pseudo-first-order kinetics, where N-CDs exhibited the highest potential for toluidine blue degradation. Our results highlight that the photocatalytic activity of carbon nanomaterials is a multifactorial process essentially driven by the formation of OH radicals, where doping and particle morphology also play a combined role in photocatalysis. This work opens a route for understanding the chemical composition and structure of photocatalytic nanocarbons and their application to the degradation of organic pollutants in water, thus offering a sustainable alternative for wastewater treatment.

Received 13th April 2025,
Accepted 16th June 2025

DOI: 10.1039/d5cy00457h

rsc.li/catalysis

Published on 04 Juli 2025. Downloaded on 18.02.26 12:30:05.

1. Introduction

The remarkable growth in research on nanocarbons is undoubtedly driven by the unique properties of these nanostructures. More than 20 years after the breakthroughs of graphene, graphene oxide, and carbon nanotubes, the scientific community is now witnessing a new revolution in non-traditional nanocarbons. In recent years, the diverse

[a] *Instituto Superior de Tecnología y Ciencias Aplicadas (InSTEC), Universidad de La Habana, La Habana, CP 10600, Cuba*
[b] *Laboratorio de Bioinorgánica, Departamento de Química General e Inorgánica, Facultad de Química, Universidad de La Habana, La Habana, C.P. 10400, Cuba*
[c] *Univ. Lille, CNRS, UMR 8516, LASIRe, F-59000 Lille, France*
[d] *Centro de Aplicaciones Tecnológicas y Desarrollo Nuclear (CEADEN), Miramar C. P. 11300, La Habana, Cuba. E-mail: luisfelipedesdingarcia@gmail.com*
[e] *Centro de Estudios Avanzados de Cuba, La Habana, Cuba*
[f] *Department of Chemistry and Chemical Biology, McMaster University, 1280 Main Street West, Hamilton, Ontario, L8S 4M1 Canada*
[g] *Brockhouse Institute for Materials Research, McMaster University, 1280 Main Street West, Hamilton, ON L8S 4M1, Canada*
[h] *National Institute of Optics, National Research Council (INO-CNR), Via Nello Carrara 1, 50019 Sesto Fiorentino, Italy*
[i] *Unité Chimie et Procédés (UCP), Ecole Nationale Supérieure de Techniques Avancées (ENSTA), Institut Polytechnique de Paris, 828 Boulevard des Maréchaux, 91120, Palaiseau, France*
[j] *Department of Functional Materials and Catalysis, Faculty of Chemistry, University of Vienna, Währinger Str. 42, 1090 Vienna, Austria*
[k] *Vienna Doctoral School in Chemistry (DoSChem), University of Vienna, Währinger Str. 42, 1090 Vienna, Austria*
[l] *Institute of Material Chemistry and Research, Faculty of Chemistry, University of Vienna, Währinger Str. 42, 1090, Vienna, Austria*
[m] *Univ. Lille, CNRS, Centrale Lille, Univ. Artois, UMR 8181, UCCS, Unité de Catalyse et Chimie du Solide, Lille F-59000, France. E-mail: manuel.antuch@centralelille.fr*

† Electronic supplementary information (ESI) available: Characterization of the solar simulator; additional XPS data; additional photodegradation experiments and kinetic information. See DOI: https://doi.org/10.1039/d5cy00457h

Published on 04 Juli 2025. Downloaded on 18.02.26 12:30:05.

applications of these materials have put them in the spotlight of attention[1] due to the large areas being impacted, such as catalysis,[2] bioimaging,[3–6] sensing,[7–11] electronic applications,[12] pharmaceuticals,[13,14] and many others.[15–17] Specifically, carbon dots (CDs) have exhibited unprecedented properties, combining high water dispersion,[15] photostability,[18] low toxicity[19] and large surface area,[17] which has enabled their use in multiple applications involving charge transfer,[20] and makes them a sustainable substitute to semiconducting materials.

The most commonly used carbon nanostructures, *e.g.*, graphene,[21] carbon nanotubes,[22] fullerenes,[23] carbon nano-onions,[24] or nanodiamonds,[25] have well-established theoretical structures, and can be obtained with a certain degree of purity. In contrast, in the case of CDs, there is no clear consensus on appropriate structural models for their representation. This is the case of carbon dots,[26] whose fluorescent properties are one of the most distinguishing features.[7] Concerning the classification of non-traditional nanocarbons such as CDs, it is worth noting that, to date, there is no general classification as a result of their structural diversity.[27] It has been expressed that CDs include nanocarbons with at least one dimension lower than 10 nm,[28] which will be the criterion followed in this paper to classify CDs as such.

Several methods have been developed for the synthesis of CDs, including laser ablation,[29,30] microwave irradiation,[31,32] chemical synthesis,[33] electrochemical synthesis,[34] pyrolysis,[35,36] and hydrothermal treatment.[2,37] Furthermore, doping of CDs with heteroatoms (*e.g.*, nitrogen, sulfur, and/or phosphorus) has been proposed to modify their peak emission wavelength and increase their quantum yield.[32,38,39] Although it is known that the maximum emission wavelength of CDs is highly dependent on the synthesis conditions, a systematic characterization of the impact of the chemical composition of such materials on their electronic and optical properties is still required, which could have important implications on their performance in various applications.

The photocatalytic application of CDs is of utmost importance and has been tuned *via* the incorporation of dopants within the carbon network. Examples of doping of such carbon nanostructures comprise elements such as N,[40] N and P;[41] N and S;[42] N, S, and P;[43] or N and B[44] along with the fabrication of composites with inorganic nanomaterials.[1,45] The effect of doping upon photocatalysis has remained a matter of active interest.[46] Some trends have been reported for specific cases, such as the decrease in photocatalytic activity upon the increase in N content, as demonstrated for a set of different organic reactions (photocatalytic dehalogenation of α-bromoacetophenone, photocatalytic oxidative coupling reaction of amines to imines, photooxidation reaction of sulfides to sulfoxides, and cross-dehydrogenation coupling).[47] On the other hand, a different study determined that both high and very low N contents caused the location of N dopants at edge sites of the C scaffold, permitting an improved photocatalytic activity towards H_2 production.[48] This variety of results in photocatalytic trends reflects the effect of structural complexity and diversity of CDs, and justifies the continued research in the field to establish all the possible parameters that could affect photocatalysis.

In particular, CD photoactivity has been exploited to degrade persistent organic dyes in wastewater from various industries, which is indeed a major environmental problem as such compounds alter the water quality of rivers, lakes, and other water bodies.[49,50] Persistent organic dyes can be toxic to aquatic organisms, affecting their survival and the ecosystem, and contaminating drinking water used in daily life. Organic dyes introduce problems to wastewater treatment because of their low biodegradability. Their hazardous potential and chemical inertia stem from the fact that their structure is formed by stable aromatic rings.[51] To overcome this environmental problem, the use of CDs and other nanocarbon structures offers a promising route to drive wastewater technologies based on photocatalytic degradation. Regarding a broader context, the integration of CDs in existing water treatment technologies bears the potential to revolutionize water purification due to their photocatalytic activity, their low toxicity, and biocompatibility. Indeed, the possibilities to provide low-cost and scalable solutions by minimizing secondary pollution[52,53] by the nanomaterial itself are an appealing alternative for the broad access to clean water, with particular importance for developing countries. The use of these innovative materials would enable a safer environment for the generations to come.

Herein, we focused on the application of carbon nanomaterials (CNs) as photocatalysts, aiming at the evaluation of their potential for the degradation of persistent organic compounds. We intend to establish the effect of doping of carbon nanostructures with heteroatoms on the observed photocatalytic activity. Therefore, we have synthesized carbon nanomaterials doped with heteroatoms: (i) N, (ii) N and S, (iii) N and P, and (iv) N, S, and P. N-doping resulted in materials with sizes below 10 nm and therefore will be referred to as carbon dots (N-CDs);[28] in cases (ii)–(iv), the multi-doped samples showed notable aggregation and larger sizes of around 100 nm and were thus defined as carbon nanomaterials (CNs). To evaluate the photocatalytic activity of such nanocarbons, we selected toluidine blue (TB) as a model pollutant not only because of its photostability, but also due to its genotoxic effects.[54,55] One major benefit of this approach is that CNs can be produced quickly and inexpensively without relying on environmentally hazardous organic solvents. This enables gram-scale synthesis under mild conditions with simple procedures, while also preventing the formation of toxic intermediates.

2. Experimental section

2.1. Chemicals

Sodium citrate, urea, cysteine, phosphoric acid, toluidine blue, Brilliant green, and Lauth's violet were purchased from

 This journal is © The Royal Society of Chemistry 2025

Published on 04 Juli 2025. Downloaded on 18.02.26 12:30:05.

MERCK; Brilliant blue and Victoria blue were obtained from SERVA and BDH, respectively. All chemicals were of analytical grade and used without further purification.

2.2. Instrumentation

High-resolution transmission electron microscopy (HR-TEM) was performed in a Thermo Fisher Scientific Talos 200X operated at 200 kV. The solutions were sonicated, drop-cast on carbon-supported TEM grids, and air-dried.

Attenuated total reflectance Fourier transform infrared (ATR-FTIR) spectra were recorded on a Varian 670-IR spectrometer (Varian, Madrid, Spain) equipped with a Golden Gate ATR model in a 4000–600 cm^{-1} range, with a spectral resolution of 4 cm^{-1} at 2000 cm^{-1}; each spectrum was averaged over 32 scans. The background ATR-FTIR was collected with the ATR crystal exposed to air.

X-ray photoelectron spectroscopy (XPS) (Nexsa, Thermofisher) was performed using Al Kα radiation at 72 W and a pass energy of 200 eV, a spot size of 400 μm, "standard lens mode", constant analyzer energy (CAE) Mode. An integrated flood gun was used to eliminate charge build-up at the surface of the sample. High-resolution spectra (step size of 0.1 eV) of the single elements were acquired with 30 passes at a pass energy of 50 eV. Samples were analysed before and after the surface treatment, which was performed by cluster Ar (1000 Ar atoms having 6000 eV) ion beam etching for 30 s. Peak analysis was performed with Thermo Avantage v5.9931 Build 06755.

Ultraviolet-visible (UV-vis) absorption spectra were recorded between 400 and 700 nm in quartz cuvettes of 1 cm optical path in an Ultrospec 2100 Pro spectrophotometer from Amersham BioSci, coupled to a computer with WaveScan software.

The fluorescence spectra were obtained using a Varian Cary Eclipse spectrofluorimeter from Agilent Technologies (Las Rozas, Madrid, Spain) equipped with an Xe flash lamp. Absorption and fluorescence spectra were recorded using quartz cuvettes with 1 cm of optical path. The quantum yield (QY) of fluorescence of each sample was collected by an absolute measurement system on an FS5 fluorimeter (Edinburgh Instruments, Livingston, UK) equipped with an integrating sphere module, comprised of a hollow sphere of 150 mm diameter with the inner surface machined from a PTFE-based material for optimum reflectance and FluOracle® software (Livingston, UK).

Continuous wave (CW) electron paramagnetic resonance (EPR) spectra were recorded at room temperature at 9 GHz with a microwave power of 2 mW and an amplitude modulation of 0.8 G. Sample irradiation was realized directly inside the cavity. The spin trapping experiment was performed using DMPO (5,5-dimethyl-1-pyrroline *N*-oxide) freshly prepared to a final concentration of 100 mM.

2.3. Synthesis of carbon nanostructures

Doped CNs were prepared using an adaptation of a microwave-assisted method, as previously reported.[56] Sodium citrate was employed as a carbon precursor, while urea, cysteine, and phosphoric acid were used as sources of nitrogen, sulfur, and phosphorus dopants, respectively. For the synthesis of CNs, the precursors were dissolved in 5.5 mL of distilled water and then heated in a 900 W microwave for 35 s. For the synthesis of N-doped CNs (N-CDs), 1 g of sodium citrate and 1 g of urea were employed; for the preparation of N,S-doped CNs (N,S-CNs), 1 g of sodium citrate and 1 g of urea and 0.125 g of cysteine were used; for the synthesis of N,P-doped CNs (N,P-CNs), 1 g of sodium citrate, 1 g of urea and 260 μL of phosphoric acid (99%) were used; for the preparation of N,S,P-doped CNs (N,S,P-CNs), 1 g of sodium citrate, 1 g of urea, 0.125 g of cysteine, and 260 μL of phosphoric acid (99%) were employed.

The dark-brown solid obtained was dried at 60 °C under vacuum to remove the remaining small molecules. Then, it was dissolved in double-distilled water and centrifuged at 4000 rpm for 20 minutes to remove large aggregates. The dispersion of CNs was then filtered over 0.45 μm membranes. The N-CDs solution was diluted and stored at room temperature.

2.4. Dye photodegradation

The photocatalytic experiments were carried out using a General Electric Quartzline Projection Lamp DYS/DYV/BHC, 600 W, 120 V, calibrated using an Avantes Starline spectrometer. The lamp irradiance for the photocatalytic experiments was adjusted to 33 mW cm^{-2}. The emission spectrum of the lamp employed in this work, and its comparison to the solar spectrum, are reported in Fig. S1.†

To evaluate the photostability of the model pollutants, the following dyes were tested: Brilliant green (BG), $C_{27}H_{34}N_2O_4S$; Lauth's violet (LV), $C_{12}H_{10}ClN_3S$; Brilliant blue (BB), $C_{45}H_{44}N_3NaO_7S_2$; Victoria blue (VB), $C_{33}H_{32}ClN_3$; and toluidine blue (TB), $C_{15}H_{16}ClN_3S$. Control experiments in the dark for each photocatalyst (N-CDs; N,S-CNs; N,P-CNs; and N,S,P-CNs) and TB were carried out under the same conditions described above, but without illumination.

Photodegradation experiments were repeated three times and took place in acrylic spectrophotometry cuvettes with a maximum capacity of 1.5 mL. Stock solutions of each photocatalyst (N-CDs, N,S-CNs; N,P-CNs and N,S,P-CNs) were prepared by dispersing 450 mg of the CNs in 20 mL of double-distilled water (ρ = 22.5 mg mL^{-1}).

To evaluate the effect of catalyst dosage, the experiment was performed at the same irradiance for each photocatalyst (N-CDs, N,S-CNs; N,P-CNs and N,S,P-CNs) but with different catalyst concentrations of 2 mg mL^{-1}, 3 mg mL^{-1}, 4 mg mL^{-1}, and 5 mg mL^{-1}, and a constant TB concentration. To determine the effect of dye concentration, the experiment was repeated using a concentration 3 mg mL^{-1} of each photocatalyst but with different TB concentrations of 45 μg mL^{-1} (1.47×10^{-7} M), 55 μg mL^{-1} (1.80×10^{-7} M), 65 μg mL^{-1} (2.13×10^{-7} M), and 75 μg mL^{-1} (2.45×10^{-7} M). The samples

Published on 04 Juli 2025. Downloaded on 18.02.26 12:30:05.

were irradiated for 90 min, and the absorbance was measured at 622 nm at 10 min intervals.

The percent photodegradation efficiency was calculated by the following equation:

$$\% \text{ normalized concentration} = (C_t/C_0) \times 100.$$

3. Results and discussion

3.1. Characterization of doped CNs

The preparation of CNs followed a microwave-assisted approach using urea and sodium citrate as the key components for doping with N and O. For the inclusion of other heteroatoms, such as sulfur and phosphorus, cysteine and phosphoric acid were also included in the reaction mixture, respectively (Scheme 1).

Initial characterization of the CNs was carried out using HR-TEM (Fig. 1). As expected, the use of urea and sodium citrate yielded small carbon dots with a size lower than 10 nm (N-CDs).[56] Overall, the nitrogen-doping (N-CDs) synthesis ensured the formation of the nanoparticles with sizes below 100 nm (Fig. 1a). Conversely, N,S-CNs formed aggregates of around 500 nm (Fig. 1b). Such aggregates displayed concentric structures that resemble onion-like carbon nanostructures. The N,P-CN samples showed, on the other hand, nanoparticles with sizes around 100 nm (Fig. 1c). Finally, the N,S,P-CNs exhibited a more defined square shape (Fig. 1d). The analysis of these results suggests a correlation between the composition and the morphology of the nanostructures, in which the presence of heteroatoms such as S and P drove the aggregation of the resulting nanoparticles.

A more detailed analysis of the TEM images provided further insights into the structure of the carbon nanostructures (Fig. 2). Fig. 2a shows a non-aggregated nanoparticle corresponding to the N,P-CNs system, where different and coexisting domains of amorphous and crystalline carbon are visible. Further magnification of Fig. 2a (Fig. 2b and c corresponding to the squares labeled with numbers 1 and 2, respectively) allowed to appreciate in more detail the co-existing crystalline structures. The interplanar distance shown in Fig. 2b corresponded to 0.7 nm, which is consistent with multilayer graphene oxide.[57,58] On the other hand, the interplanar distance observed in Fig. 2c was 0.3 nm and was attributed to the (002) plane of graphite.[58,59] Nanodiamond domains show a plane separation of 0.2059 nm for the (111) lattice plane,[59] and were not found in the structure of this N,P-CNs particle. This was expected considering that nanodiamonds are formed under far more extreme detonation conditions.[60]

Additional characterization of the carbon materials was carried out using ATR-FTIR to examine the functional groups grafted on the samples (Fig. 3). For all samples, the bands observed from 3500 to 3200 cm^{-1} correspond to the stretching vibration of –OH, –COOH, and $–NH_2$ groups. These functional groups were responsible for the high water dispersibility of all CNs studied. The peak observed at 2248 cm^{-1} in the spectra of N-CDs and N,S-CNs was attributed to the stretching vibration of –NCO bonds, which suggested the presence of the isocyanate group. Additionally, the peaks at 1750–1600 cm^{-1} resulted from the stretching vibrations of

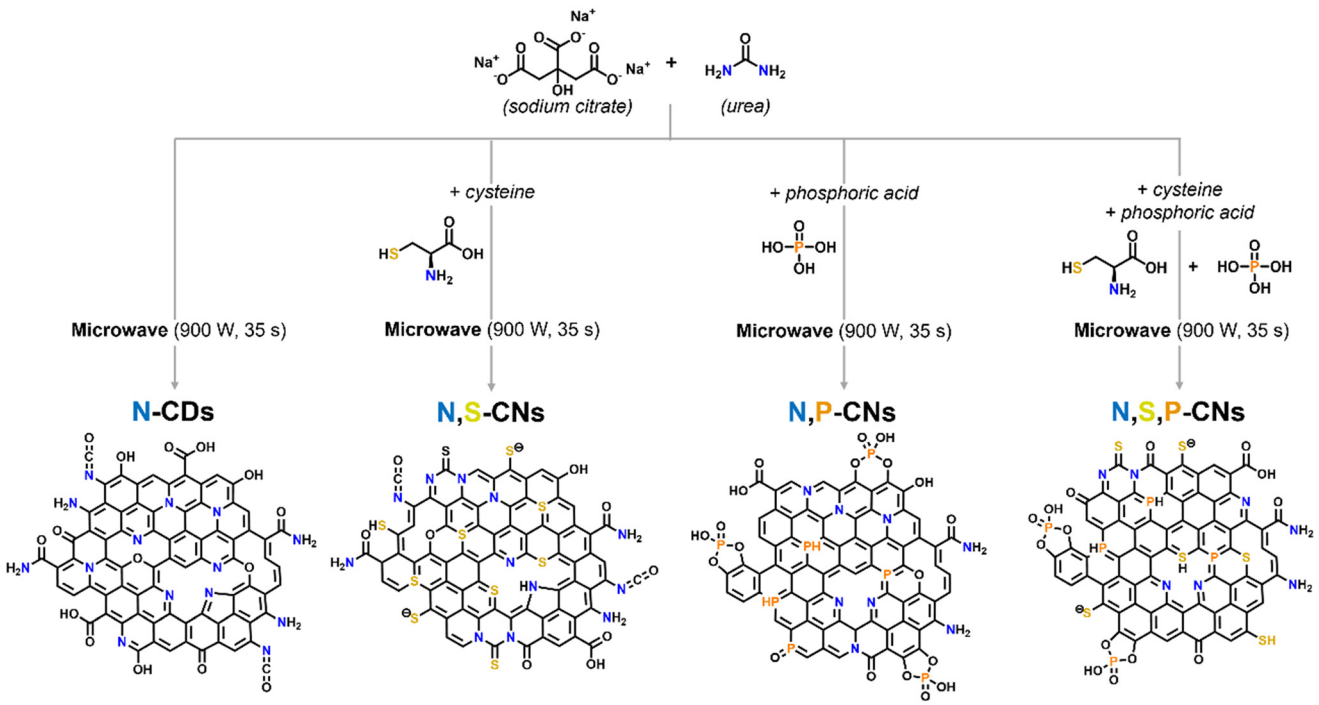

Scheme 1 Methodology for the synthesis of the multi-doped carbon nanomaterials: N-CDS; N,S-CNs; N,P-CNs; and N,S,P-CNs.

 This journal is © The Royal Society of Chemistry 2025

Published on 04 Juli 2025. Downloaded on 18.02.26 12:30:05.

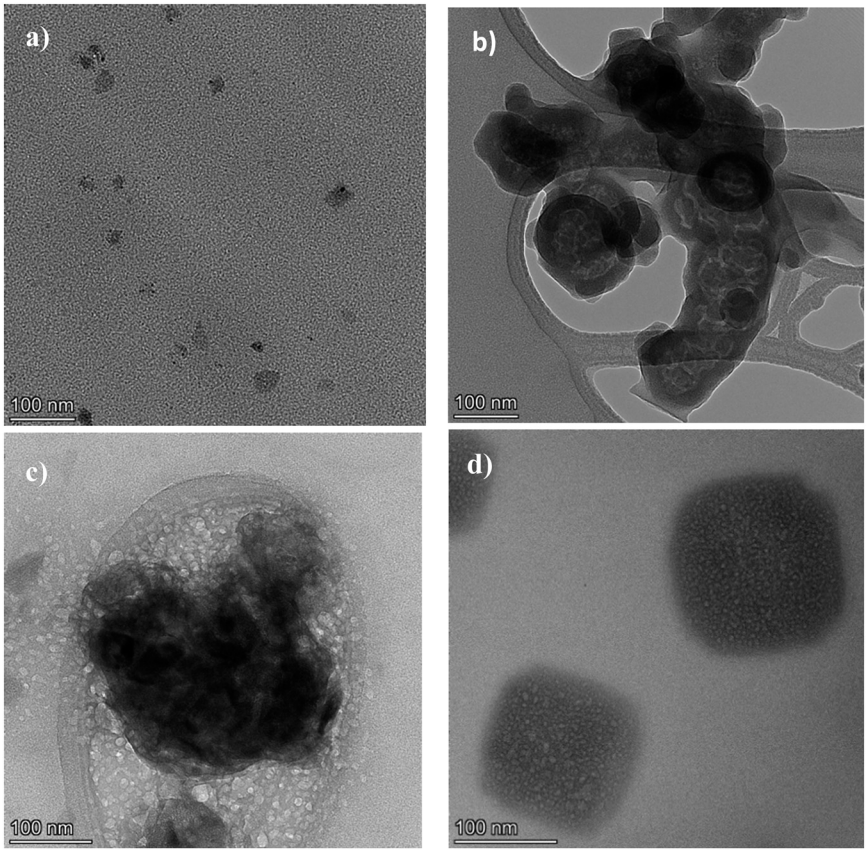

Fig. 1 Transmission electron microscopy images of (a) N-CDs (b) N,S-CNs, (c) N,P-CNs (d) N,S,P-CNs.

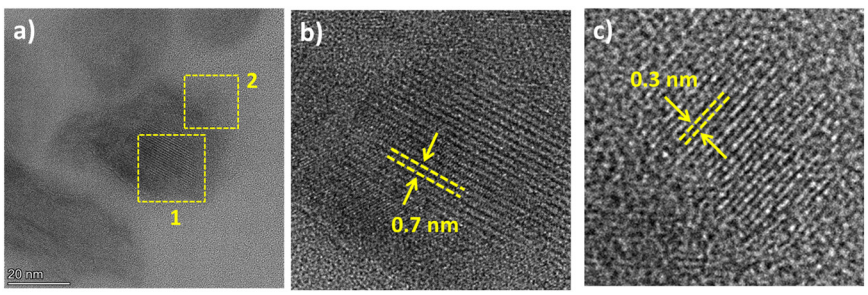

Fig. 2 (a) Magnified TEM image of a non-aggregated N,P-CNs nanoparticle; (b) magnification of the square labeled as 1 in Fig. 2a, where interlayer spacing of graphene oxide is appreciated; (c) magnification of the square labeled as 2 in Fig. 2a, where interlayer spacing of graphite is appreciated.

C═C and C═O bonds from the CNs, typical of their conjugate structure of all the CNs. The sharp signals around 1580–1500 cm^{-1} and 1380 cm^{-1} were attributed to the stretching vibration of C–N and bending vibration of NH_2, respectively, indicating the N-doping. In the case of N,S,P-CNs, the spectrum exhibited a peak at 1130 cm^{-1}, which is attributed to the P═O stretching and was also visible in the N,P-CNs spectrum. Moreover, for these P-doped samples, a band at 910 cm^{-1} was observed and assigned to P–O–R moieties, where R stands for an aromatic structure.[41,61] Overall, these results indicated the success of doping in all the synthesized materials.

High-resolution X-ray photoelectron spectroscopy (XPS) characterization (Fig. 4) aligned with the FTIR data (Fig. 3) and provided detailed insights into the chemical composition of the doped-carbon materials (Table S1†). The atomic content of N (%) in all the samples was comparable (17–18%), while the detection of 2.5% (N,S-CNs) and 1.6% (N,S,P-CNs) of sulfur, as well as 1.1% (N,P-CNs) and 0.5% (N,S,P-CNs) of phosphorous in the multi-doped samples further validated the successful incorporation of the heteroatoms into the carbon framework.

The binding energy scales were calibrated to the C 1s standard value of 284.8 eV, and the fitted C 1s spectra were

Published on 04 Juli 2025. Downloaded on 18.02.26 12:30:05.

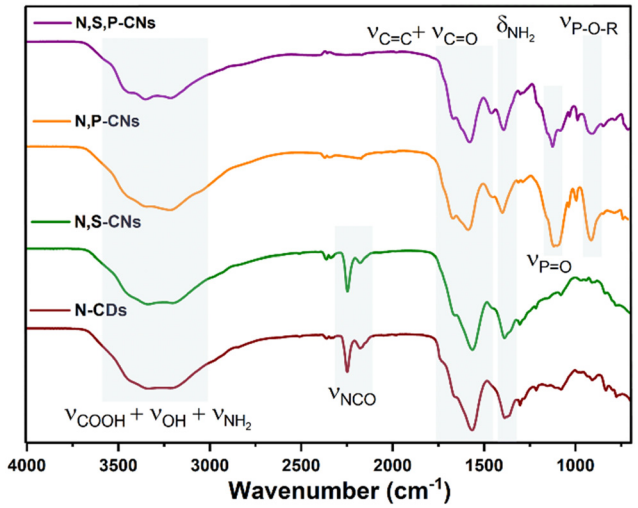

Fig. 3 FT-IR spectra of the doped carbon nanostructures.

deconvoluted into three signals (Fig. S2†), corresponding to carbon in the form of C═C/C–C bonds (~284.8 eV), C–O/C–N (~286.1 eV), and C═O/C═N (~288.1 eV).[62,63] The O 1s band was fit into three peaks (Fig. 4a), which were found at

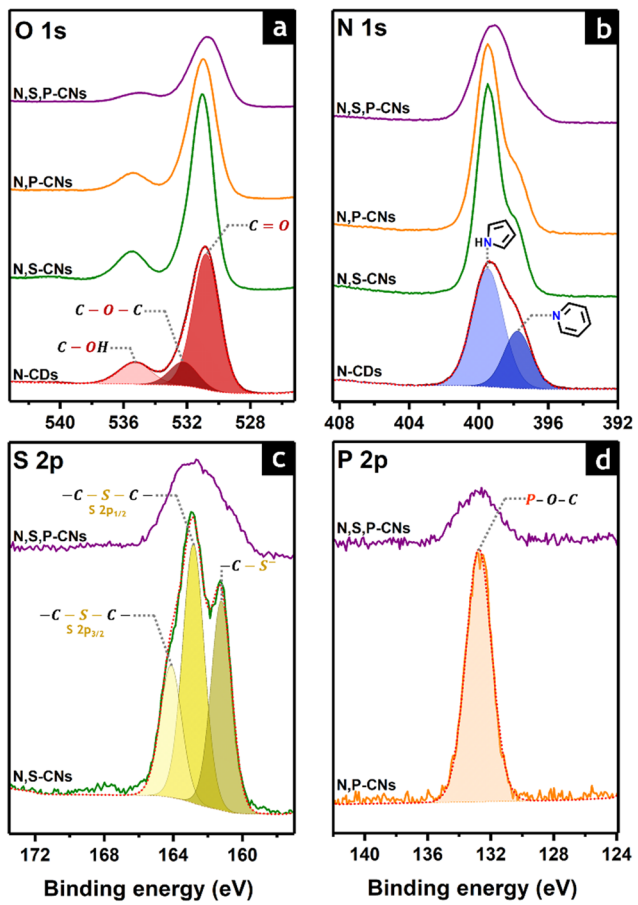

Fig. 4 High-resolution XPS spectra depicting O 1s (a), N 1s (b), S 2p (c), and P 2p (d) orbital binding energy regions for doped carbon nanostructures.

530.9 eV, 532.3 eV, and 535.3 eV and assigned to C═O, C–O–C, and C–OH functions, respectively.[63,64] The presence of pyridinic and pyrrolic nitrogen in all the doped materials was confirmed by analyzing the deconvoluted N 1s spectra (Fig. 4b), which exhibited the typical peaks at 397.7 eV and 399.4 eV, respectively.[63,65] Interestingly, the relative composition of pyridinic N in the samples decreased from 30.2% in N-CDs to 20.8%, 20.1%, and 11.4% in N,S-CNs, N,P-CNs, and N,S,P-CNs, respectively (Table S2†), with a corresponding increase in pyrrolic N. Furthermore, the deconvoluted S 2p spectra of N,S-CNs and N,S,P-CNs (Fig. 4c) revealed S $2p_{3/2}$ and S $2p_{1/2}$ spin–orbital split signals at 162.9 eV characteristic of C–S–C,[66] along with an additional peak at 161.2 eV, which suggested the formation of organic thiolates upon sulfur doping. In contrast, a main peak in the P 2p spectra of N,P-CNs and N,S,P-CNs was observed at 132.8 eV, indicative of P–O–C species.

The samples were additionally characterized by UV-visible spectroscopy to explore the optical properties of the carbon materials obtained. As depicted in Fig. 5a, all samples exhibit similar UV-vis spectra with an absorption band centered at 328 nm, corresponding to the n–π* transition of C═O from carboxyl groups present on the samples. The band observed at 400 nm was attributed to n–π* transitions[67] and showed a bathochromic shift compared to the typical carbonyl transitions. This is due to the extended conjugation in unsaturated motifs within the nanocarbon structures. The π–π* transitions corresponding to the C–C conjugate characteristic structure of CDs appeared as an absorption tail below 275 nm.[61]

To deepen the understanding of the optical properties of the CNs, the fluorescence of the materials was additionally evaluated (Fig. 5b), confirming a high emission signal for all the samples obtained. For an excitation wavelength of 348 nm, the emission wavelength was found at 438 nm for N-CDs and N,S-CNs. On the other hand, for N,P-CNs and N,S,P-CNs, the emission bands were observed at 434 nm and 440 nm, respectively. The fluorescence quantum yield (QY) values corresponded to 5.58% for N-CDs, 4.35% for N,S-CNs, 4.93% for N,P-CNs, and 3.66% for N,S,P-CNs. These QY values are typical of carbon dots prepared using urea and citric acid.[68] The slightly larger QY value in N-CDs was aligned with a more efficient use of the adsorbed light by these nanostructures, thus suggesting a greater photocatalytic activity. The origin of the fluorescence in carbon dots, and extensively in carbon nanomaterials, has been attributed to three main effects, namely (i) molecular fluorescence, (ii) quantum confinement, and (iii) the presence of surface states due to surface oxidation and the presence of functional groups.[69] All these factors and their synergistic interaction have been thoroughly discussed before.[69] In the case of the nanostructures obtained in this work, both their size (Fig. 1) and the presence of multiple functional groups (Fig. 3 and 4) justify the optical properties illustrated in Fig. 5.

This journal is © The Royal Society of Chemistry 2025

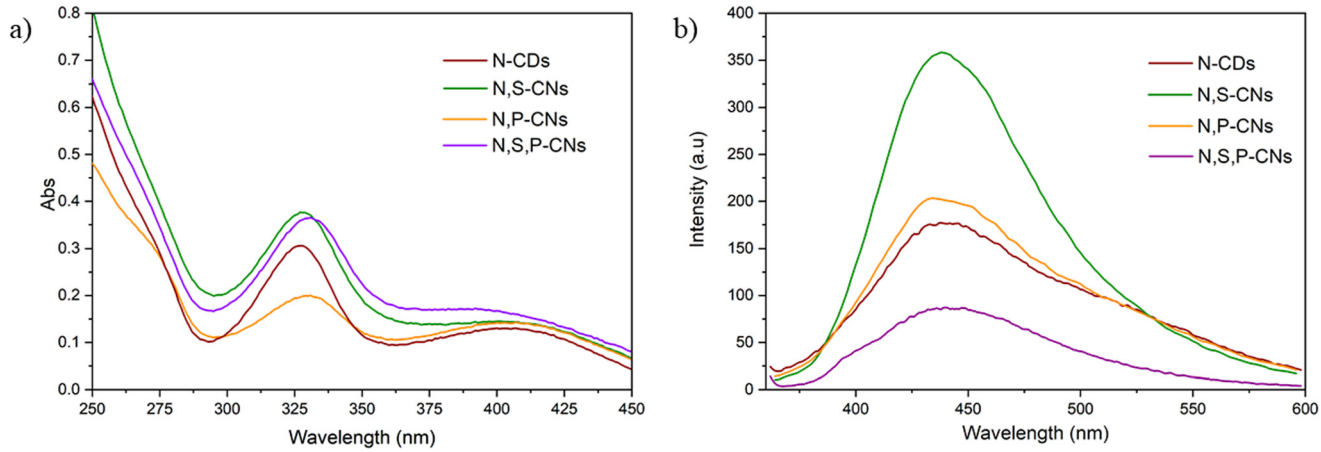

Fig. 5 (a) UV-vis and (b) fluorescence spectra of each CNs, excitation wavelength of 348 nm.

Published on 04 Juli 2025. Downloaded on 18.02.26 12:30:05.

3.2. Application of N-CDs, N,S-CNs, N,P-CNs, and N,S,P-CNs as photocatalysts in the photodegradation of toluidine blue

Once the structural, chemical, and optical properties of the carbon nanomaterials were assessed, we proceeded to evaluate their potential as photocatalysts in the presence of visible light. For the photocatalytic experiments, we employed a solar simulator, whose characteristics are depicted in Fig. S1.† It is worth highlighting that the solar simulator showed a close resemblance to the Reference Air Mass 1.5 Spectra,[70] which is desirable to test photocatalytic procedures in conditions as close as possible to natural irradiation.

For the selection of the model pollutant in degradation experiments, we tested the photostability of several dyes in the absence of the carbon nanostructures (Fig. S3†). In particular, TB showed higher stability against light when compared to the other compounds tested, since less than 5% of the dye was degraded during constant irradiation for 160 min, and for this reason, it was used for photocatalysis experiments with the doped CNs. As an additional control, TB was put in contact with all the carbon nanostructures in the dark, and less than 5% of TB was degraded in such conditions, indicating the role of light in driving the photocatalytic activity of the samples (Fig. S4†).

Typical UV-vis spectra for the degradation of TB in the presence of N-CDs are shown in Fig. 6a, where a systematic decrease in the band intensity at 600 nm is observed, consistent with the photodegradation of the dye upon continuous irradiation in the presence of visible light during 90 minutes. The time-dependent photodegradation of TB, photocatalyzed by each of the doped nanostructures, is shown in Fig. 6b and c. The N-CD catalysts enabled degradation of 66 ± 4% of the TB after 90 min of irradiation. On the other hand, when the N,S-CNs catalyst was used, 51 ± 2% of the initial concentration of TB was lost, as was the case for the N,P-CNs, which also degraded 51 ± 2% under the same experimental conditions. Finally, the N,S,P-CNs showed

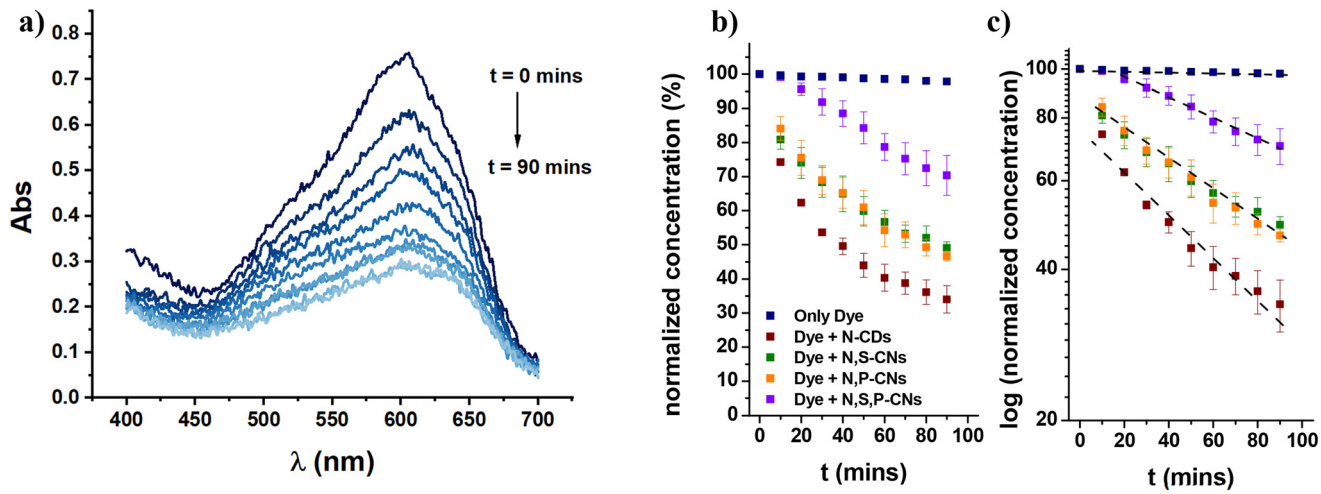

Fig. 6 (a) Typical UV-vis spectra for the degradation of toluidine blue in the presence of N-CDs. (b) Time evolution of the normalized concentration of toluidine blue upon irradiation with visible light in the presence of different carbon nanostructures. (c) Pseudo-first-order kinetics for dye degradation. Error bars correspond to three independent experiments.

Published on 04 Juli 2025. Downloaded on 18.02.26 12:30:05.

the lowest photocatalytic activity, degrading only 30 ± 4% of the TB. In this regard, doping with heteroatoms not only decreases the band gap but also introduces additional energy levels into the carbon nanostructure. These energy levels can facilitate charge transfer and electron–hole separation, fundamental processes in the generation of photogenerated electron–hole pairs involved in photocatalysis processes.[40] While recent literature reports suggest that incorporating heteroatoms in CNs should lead to more efficient photocatalytic activity,[71] our experimental observations show a different trend. This could be because a broad range of morphologies was obtained. Indeed, the agglomeration of the multi-doped samples (N,S-CNs, N,P-CNs, and N,S,P-CNs) might also have resulted in the lower catalytic efficiency of such materials in comparison to the nano-sized carbon dots (N-CDs). The lowest photodegradation efficiency of N,S,P-CNs is in agreement with a previous report where such material was used as a photocatalyst under UV light, and modest photocatalytic efficiency was observed.[43] Thus, our results, analyzed in the context of existing literature,[43,71] suggest that photocatalysis of carbon nanostructures is a complex phenomenon where doping is important but not the only factor at stake, such as nanoparticle size and morphology, which seems to be the reason behind the activity trend observed in this work.

The mechanism of carbon nanomaterials-assisted photodegradation is likely to follow the generation of reactive oxygen species.[72] Indeed, when a photocatalyst is exposed to visible light, charge separation occurs, and the photogenerated electron–hole pairs are created. The resulting electrons could react with dissolved oxygen molecules, giving rise to superoxide anions, whose dismutation may result in hydrogen peroxide and water. On the other hand, oxidizing holes may react with water molecules in order to generate hydroxyl radicals in diverse photocatalytic materials.[45,73] It has been established that the presence of functional groups in carbon dots may be correlated to the apparition of reactive oxygen species; in particular, hydroxyl radicals,[72,74] which are typically formed in visible-light-driven reactions.[75–77] Inspired by such reported results, we undertook electron paramagnetic resonance (EPR) experiments to determine the nature of the reactive intermediates responsible for the observed photocatalytic activity using N-CDs, which showed the highest photodegradation capabilities among all materials obtained. Without irradiation, no EPR signal was detected (Fig. 7a, black line), whereas upon irradiation, the formation of two radical species could be detected after 40 s (Fig. 7a, red line). The three lines observed in the spectrum (g = 2.005) were attributed to an electron coupling with nitrogen (nuclear spin for N has a value of I = 1, and the peak multiplicity equals $2nI + 1 = 3$). A second species (g = 2.0028) with a weak anisotropy was additionally observed and attributed to an oxygen-centered radical. The N-centered radical disappeared beyond the 40 s, but the O-centered radical remained stable throughout the irradiation time, as observed upon 1 h-irradiation (Fig. 7a, green line). The same experiment was then carried out with the addition of DMPO spin-trap agent (Fig. 7b), which corroborated the formation of the DMPO–OH adduct, thus confirming that the mechanism of dye degradation is likely to be mediated by the formation of the OH radical. Such an active radical is a strong oxidant, which may react with the TB dye, leading to its decomposition into water molecules and carbon dioxide. In addition to this, the light-induced holes possess a high oxidation capacity, which would also enable the direct degradation of the TB dye molecules, transforming them into innocuous by-products.[78]

3.3. Kinetics of dye photodegradation

Kinetic studies were undertaken to provide deeper insights into the photodegradation process. The kinetics of

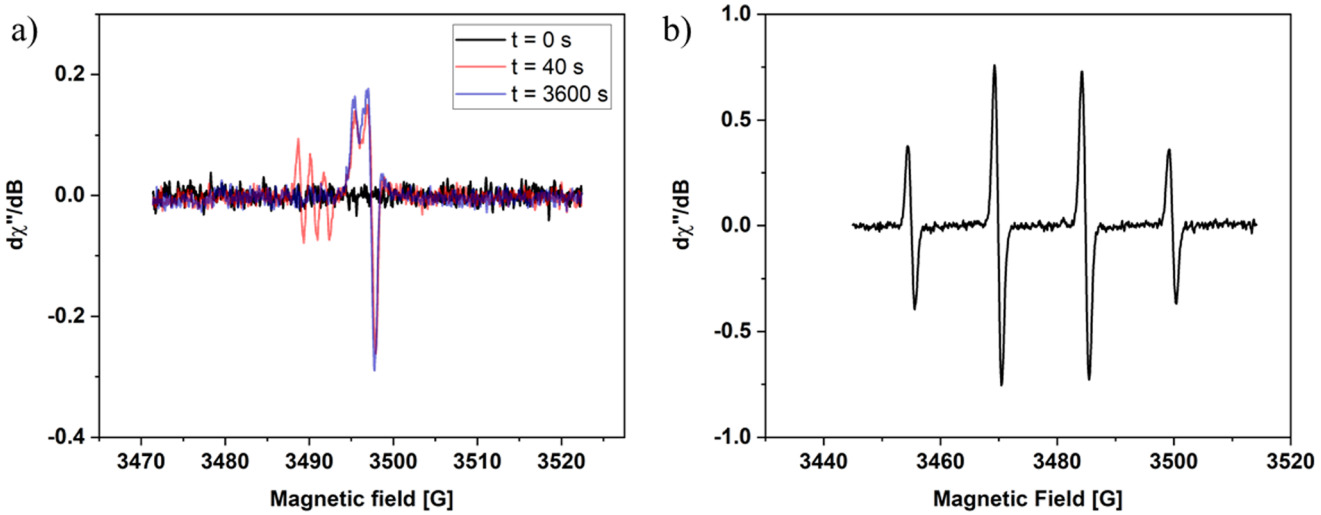

Fig. 7 (a) EPR spectra recorded at 0 s, 40 s and 3600 s; (b) the EPR spectrum corresponding to the DMPO–OH spin adduct.

 This journal is © The Royal Society of Chemistry 2025

Published on 04 Juli 2025. Downloaded on 18.02.26 12:30:05.

photocatalytic reactions is typically described using a simplified Langmuir–Hinshelwood model eqn (1),[79] taking into account the adsorption of the substrate (the dye) to the photocatalyst (the CNs), and its further transformation into a product. Such a model assumes a Langmuir isotherm (eqn (1)) for the adsorption of the substrate at the surface of the photocatalyst. The model offers a detailed description of the dynamics of the system in terms of phenomenological parameters that contain several kinetic constants accounting for the individual reaction steps and light absorption processes.[80] Two limiting cases may be identified in this model, namely (i) where the active sites of the photocatalyst are saturated and therefore the term $KC \gg 1$, implying a constant surface coverage of the substrate (θ) and pseudo-zero order kinetics; and (ii) where the product $KC \ll 1$ and thus the surface coverage of the adsorbed substrate depends linearly on the concentration and the rate follows pseudo-first order kinetics.

$$\theta = \frac{KC}{1 + KC} \quad (1)$$

$$v = k\theta = \frac{kKC}{1 + KC} \quad (2)$$

In eqn (1), θ represents the surface coverage of substrate (dye), K is the equilibrium constant associated with the adsorption of the substrate to the surface of the photocatalyst, and C represents the concentration of the substrate; in eqn (2), k stands for the rate constant of the photodegradation process. All symbols used in eqn (2) retain their significance from eqn (1).

An inspection of photocatalytic data (Fig. 6b, S5 and S7†) shows that the time evolution of the TB concentration did not follow a straight line. Thus, pseudo-zero-order kinetics was ruled out. At the same time, the linear dependence of $\ln c$ *vs.* t indicates pseudo-first-order behavior (Fig. 6c, S6 and S8†). The corresponding apparent rate constants (k, min^{-1}) are reported in Tables S3 and S4† for the different experimental conditions tested. The evaluation of the photodegradation kinetics ensured that the measurements were performed in the linear part of the adsorption isotherm (eqn (1)). Therefore, the photoactive sites of the CNs were not saturated by the dye.[80] The best performance of N-CDs was expressed not only by the largest dye photodegradation percent (Fig. 6b) but also by the largest kinetic rate constant in comparison to N,S-CNs, N,P-CNs and N,S,P-CNs at different concentrations of the catalysts (Table S3†) or TB (Table S4†).

3.4. Effect of photocatalyst and dye concentration

The TB photodegradation was optimized by varying operational parameters. This is crucial to avoid photocatalyst waste in an eventual practical application. Through this optimization, we determined the best working concentrations for all carbon catalysts (Fig. S5†). Thus, the optimal concentration for N-CDs corresponded to 3 mg mL^{-1} since the lowest concentration of remaining TB was detected for all the time-slots tested. In turn, for N,S-CNs (Fig. S5b†), and N,P-CNs (Fig. S5c†), the optimal concentrations corresponded to 3 mg mL^{-1} and 2 mg mL^{-1}, respectively. Finally, for N,S,P-CNs (Fig. S5d†), the optimal concentration was found to be 2 mg mL^{-1}. The increase of the photocatalyst concentration might have favored TB degradation because of the increase in the active sites, thus generating a higher concentration of reactive species in the medium. This was only maintained up to a certain concentration, at which the reaction rate reached a plateau or even decreased, which might be due to the increased light scattering with the increasing amount of the photocatalyst.[81]

Another critical parameter considered during optimization was the concentration of the dye (Fig. S7†), as it is crucial in wastewater treatment. Overall, a systematic decrease in the photodegradation efficiency upon increasing dye concentration was observed. This was attributed to an increased amount of light-absorbing molecules near the photocatalyst and, therefore, a lower number of photons available to excite the photocatalyst, hence decreasing the reaction rate.[81,82] Another important factor to consider would be the gradual adsorption of the dye on the photocatalyst surfaces, with the eventual formation of multilayers around the CNs that would hinder electron–hole pair formation, thus decreasing the degradation efficiency.[81,82]

3.5. Comparison to other photocatalytic systems for dye degradation

To put our results in the framework of previous studies, we have gathered a selection of relevant data in Table 1. Despite the fact that the literature shows inherent experimental variability due to the use of different light sources, the design of reaction vessels, and the catalyst loading, it is useful to analyze the results of this work in the frame of existing photocatalytic systems for dye degradation. For example, the degradation percentage and the rate constant for dye degradation catalyzed by the CNs obtained are comparable to previous studies, falling within the order of 10^{-2} min^{-1}. What is relevant, though, is that we could demonstrate that the use of carbon nanomaterials, especially N-doped carbon dots (N-CDs), improved the rate of dye degradation by a factor of 100 (as obtained by dividing the rate constant for TB dye alone and that obtained using N-CDs). Our results are remarkable when compared to the 1.4 rate increase (for methylene blue) or 2.8 rate increase (for malachite green) reported in ref. 83. Concerning the TB dye, the rate constant reported in this work is superior to the values reported in the literature, which fall in the order of 10^{-3} min^{-1}.[79,84] It is worth highlighting that in ref. 40, the authors used H_2O_2 to boost the photodegradation kinetics and catalyst efficiency, which was not necessary for the photodegradation reported in our study. Even in the absence of H_2O_2, our materials exhibited a

Published on 04 Juli 2025. Downloaded on 18.02.26 12:30:05.

Table 1 Comparison of the dye breakdown efficiency of work with existing literature

Material	Organic dye	Light source	Degradation efficiency	Irradiation time (min)	Rate constant (min^{-1})	Ref.
—	Toluidine blue	Visible light (1/3 sun)	2%	90	$(1.4 \pm 0.7) \times 10^{-4}$	This work
N-CDs	Toluidine blue	Visible light (1/3 sun)	66 ± 4%	90	$(1.1 \pm 0.1) \times 10^{-2}$	This work
N,S-CNs	Toluidine blue	Visible light (1/3 sun)	51 ± 2%	90	$(0.70 \pm 0.06) \times 10^{-2}$	This work
N,P- CNs	Toluidine blue	Visible light (1/3 sun)	51 ± 2%	90	$(0.80 \pm 0.05) \times 10^{-2}$	This work
N,S,P-CNs	Toluidine blue	Visible light (1/3 sun)	30 ± 4%	90	$(0.40 \pm 0.02) \times 10^{-2}$	This work
NSP-CNs	Methylene blue	Low-pressure mercury lamp (20 W, λ = 254 nm)	0%	150	—	43
TiO_2	Methylene blue	Low-pressure mercury lamp (20 W, λ = 254 nm)	51%	40	—	43
NP-GQDs-90 (phosphorus co-doped graphene quantum dots)/g-C_3N_4	Methyl orange	Xe lamp (PLS-SXE300, 300 W, $\lambda > 420$ nm)	100%	120	3.1×10^{-2}	85
g-C_3N_4	Methyl orange	Xe lamp (PLS-SXE300, 300 W, $\lambda > 420$ nm)	50%	120	6.9×10^{-3}	85
Sulphur-doped carbon quantum dots (SCQDs)	Crystal violet	UV-light	99%	200	—	86
—	Methylene blue	Sunlight	59%	180	1.28×10^{-2}	83
Nitrogen-doped carbon quantum dots (NCQDs)	Methylene blue	Sunlight	97%	180	1.79×10^{-2}	83
—	Malachite green	Sunlight	59%	120	0.68×10^{-2}	83
Nitrogen-doped carbon quantum dots (NCQDs)	Malachite green	Sunlight	98%	120	1.92×10^{-2}	83
Sulfur and nitrogen co doped graphene quantum dots (S,N-GQDs)	Crystal violet	Visible light	91%	100	—	87
Carbon quantum dots (CQDs)/$KNbO_3$	Crystal violet	Visible light	70%	300	—	88
CdS nanoparticles	Toluidine blue	—	90.9%	120	8.37×10^{-3}[a]	84
Hexamethylenetetramine zinc(II) porphyrin complex + H_2O_2	Toluidine blue	—	50%	180	3.6×10^{-3}[b]	79
MB	Methylene blue	Sunlight	79%	80	1.9×10^{-2}	89
ZnO	Methyl orange	Sunlight	87.5%	120	1.8×10^{-2}	90
ZnO	Methylene blue	Sunlight	82.2%	120	1.5×10^{-2}	90
CuO	Atrazine	UV 254 nm	45%	60	9.1×10^{-3}	91

[a] In such work, the rate constant is expressed in h^{-1} units. For the sake of simplicity to compare with the data reported in this paper (in min^{-1}), we have converted to min^{-1} the value of the rate constant reported in ref. 84, through a division by a factor of 60 of the original value reported in h^{-1}. Such a value is the largest rate constant reported in ref. 84. [b] In such work, the authors use a logarithmic plot to determine the rate constant for dye degradation and report it as if it were second-order kinetics. This is likely a typographic error, and therefore we report it here in coherence to the log plot reported by the authors in Fig. 7 within ref. 79. Note that the authors do not report on the units of the rate constant, but observing that the time span is expressed in minutes, the most likely scenario is that the units are min^{-1}.

better catalytic performance. Unfortunately, the possibility of comparison to such previous studies (ref. 79 and 84) is rather limited since in those works, the authors did not report on the characteristics of their solar simulator and the irradiance being used; suffice it to say that the degradation efficiency observed for our carbon nanostructures (see Table 1) in 90 minutes and using 1/3 sun irradiation power, is remarkable. Likewise, systems displaying kinetic data comparable to the obtained N-CDs corresponded to composites of phosphorus co-doped graphene quantum dots (NP-GQDs) and g-C_3N_4, both used for the degradation of methyl orange (ref. 85). The rate constant was well in the 10^{-2} min^{-1} order, but again, a full comparison is limited since the actual irradiance was not reported.

Conclusions

In this study, the synthesis of heteroatom-doped carbon dots (CNs) was achieved by a microwave-assisted method using sodium citrate as the carbon precursor. Extensive characterization of the doped CNs, which included techniques such as FTIR, XPS, UV-vis, and fluorescence spectroscopies, confirmed the successful doping and revealed remarkable optical properties associated with the different doping combinations (N-CDs, N,S-CNs, N,P-CNs and N,S,P-CNs). By studying the photocatalytic properties of the carbon structures, it was observed that they exhibit significant and diverse capabilities for the degradation of TB, which was related to the different composition and morphology of the carbon nanostructures. Specifically, nitrogen doping was highlighted by achieving 66% degradation of this dye within 90 minutes of irradiation, underscoring the efficacy of nitrogen-doped CDs smaller than 10 nm as effective photocatalysts in this context. In addition, the effects of catalyst concentration and dye concentration were explored, revealing that the degradation process follows pseudo-first-order kinetics. This behavior is observed in a particular case of the Langmuir–Hinshelwood mechanism, where the catalytic sites of the nanomaterials were not saturated by the dye, suggesting fast

 This journal is © The Royal Society of Chemistry 2025

Published on 04 Juli 2025. Downloaded on 18.02.26 12:30:05.

photodegradation. The best system we studied (N-CDs) places itself well within the state-of-the-art regarding the kinetics of the process, within the order of 10^{-2} min^{-1}. The mechanism of dye degradation for the most active system (N-CDs) was approached using EPR spectroscopy. Thus, the irradiation of N-CDs yielded two types of radicals centered in N (stable for around 40 s) and in O (stable during the irradiation time), proving the formation of radical species in the material. Additionally, the irradiation in the presence of the addition of the DMPO radical trap showed the formation of the hydroxyl radical, which is a highly oxidizing species responsible for the oxidation of the dye. An analysis of our results suggests that, to promote the optimal design of photocatalytic nanocarbons based on the microwave-based reaction of urea and sodium citrate, the dopant of choice is N, which results in smaller nanoparticles with improved activity. Future research directions will be associated with the exploration of synthetic conditions to achieve dispersed uniform multidoped nanoparticles with higher surface area as N-CDs, and also with the long-term application of these nanocarbons in practical technologies. These findings not only deepen the understanding of the photocatalytic properties of doped CNs, underscoring their efficacy in photocatalytic applications, but also highlight their potential to address environmental challenges, especially in terms of the degradation of pollutant dyes in wastewater.

Data availability

Data related to this work will be made available upon reasonable request.

Conflicts of interest

There are no conflicts to declare.

Acknowledgements

D. G. M. was partially supported through an Ontario Graduate Scholarship and an NSERC Vanier Canada Graduate Scholarship. J. M. M.-M. is the Tier 2 Canada Research Chair in Micro and Nanostructured Materials. The research presented was partially supported by funding through a Discovery Grant from NSERC to J. M. M.-M. (RGPIN-2019-06433). This research made use of equipment within the Canadian Centre for Electron Microscopy (CCEM) at McMaster University. C. I.-M., Q. J., and F. K. would like to thank the University of Vienna (Austria) for the financial support. M. A. is thankful to Centrale Lille Institut, to the Unité de Catalyse et Chimie du Solide, and to the Agence Nationale de la Recherche, grant ANR-23-CPJ1-0019-01, for financial support. Graphical elements included in the manuscript were created with **https://BioRender.com**.

References

1 M. C. M. D. de Conti, *et al.*, Carbon dots in the center of the spotlight: A full evaluation of their synthesis and understanding of their fundamental properties and applications, *Mater. Today Sustain.*, 2024, **27**, 100937.
2 S. Xu, Y. Wang, Y. Wu and M. Li, Nitrogen and sulfur co-doped coal-based carbon quantum dots enhance the photocatalytic hydrogen evolution of Co-Fe-P derived from MOF, *Surf. Interfaces*, 2024, **44**, 103576.
3 M. Bartkowski, Y. Zhou, N. Amin, S. J. Eustace and S. Giordani, CARBON DOTS: Bioimaging and Anticancer Drug Delivery, *Chem. – Eur. J.*, 2024, **30**, e202303982.
4 A. Tan, G. Yang and X. Wan, Ultra-high quantum yield nitrogen-doped carbon quantum dots and their versatile application in fluorescence sensing, bioimaging and anti-counterfeiting, *Spectrochim. Acta, Part A*, 2021, **253**, 119583.
5 Z. Liao, *et al.*, Covalently hybridized carbon dots@mesoporous silica nanobeads as a robust and versatile phosphorescent probe for time-resolved biosensing and bioimaging, *Analyst*, 2024, **149**, 1473–1480.
6 L. Shen, *et al.*, Switching Carbon Nanodots from Single Emission to Dual Emission by One-Step Electrochemical Tailoring in Alkaline Alcohols: Implications for Sensing and Bioimaging, *ACS Appl. Nano Mater.*, 2019, **2**, 2776–2784.
7 A. López-beltrán, *et al.*, Design of Fluorescent Carbon Dots (CDs) for the Selective detection of Metal-Containing Ions, *Chem. – Eur. J.*, 2023, **29**, e202300188.
8 X. Gao, *et al.*, Nano-biosensor based on manganese dioxide nanosheets and carbon dots for dual-mode determination of Staphylococcus aureus, *Food Chem.*, 2024, **432**, 137144.
9 W. Liu, *et al.*, A biosensor encompassing fusarinine C-magnetic nanoparticles and aptamer-red/green carbon dots for dual-channel fluorescent and RGB discrimination of Campylobacter and Aliarcobacter, *Talanta*, 2024, **266**, 125085.
10 D. H. Sandeep, *et al.*, Sustainable fabrication of fluorescent carbon quantum dots as an optical amplifier in modern agriculture, anti-counterfeiting, food packing and intelligent pH detection, *Mater. Today Sustain.*, 2024, **27**, 100855.
11 H. Dong, *et al.*, Nitrogen-doped carbon dots as green materials for sensitive and selective detection of isorhamnetin, *Mater. Today Sustain.*, 2024, **27**, 100888.
12 Y. Cao, H. Hao, L. Chen and Y. Yang, Recent advances of carbon dot-based memristors: Mechanisms, devices, and applications, *Appl. Mater. Today*, 2024, **36**, 102032.
13 Q. Meng, *et al.*, Carbon dot-modified controllable drug delivery system for sonodynamic/chemotherapy, *Mater. Chem. Front.*, 2024, **8**, 1362–1372.
14 A. Kumawat, B. Saini and C. Ghoroi, Nanodroplets Engineered with Folate Carbon Dots for Enhanced Cancer Cell Uptake toward Theranostic Application, *ACS Appl. Bio Mater.*, 2024, **7**, 5483–5495.
15 Z. Zhang, J. Zhao, X. Li and B. Wang, Materials Transforming water-soluble carbon dots with high particle size regularity as the high-performance oil-based lubricant

Published on 04 Juli 2025. Downloaded on 18.02.26 12:30:05.

additives by one-step surface modification, *Diamond Relat. Mater.*, 2024, **141**, 110715.
16 G. Yi, *et al.*, Copper Ion-Induced Self-Assembled Aerogels of Carbon Dots as Peroxidase-Mimicking Nanozymes for Colorimetric Biosensing of Organophosphorus Pesticide, *ACS Sustainable Chem. Eng.*, 2024, **12**, 1378–1387.
17 Atika and R. K. Dutta, Nucleotide-Based Carbon Dot-Assisted Synthesis of High Surface Area Porous α-Ni(OH)2 as an Efficient Battery-Type Supercapacitor Electrode, *Energy Technol.*, 2024, **12**, 2400427.
18 F. Li, D. Yang and H. Xu, Non-Metal-Heteroatom-Doped Carbon Dots: Synthesis and Properties, *Chem. – Eur. J.*, 2019, **25**, 1165–1176.
19 X. Kou, S. Jiang, S. J. Park and L. Y. Meng, A review: recent advances in preparations and applications of heteroatom-doped carbon quantum dots, *Dalton Trans.*, 2020, **49**, 6915–6938.
20 V. Magesh, A. K. Sundramoorthy and D. Ganapathy, Recent Advances on Synthesis and Potential Applications of Carbon Quantum Dots, *Front. Mater.*, 2022, **9**, 906838.
21 X. Li, J. Yu, S. Wageh, A. A. Al-Ghamdi and J. Xie, Graphene in Photocatalysis: A Review, *Small*, 2016, **12**, 6640–6696.
22 D. Tasis, N. Tagmatarchis, A. Bianco and M. Prato, Chemistry of Carbon Nanotubes, *Chem. Rev.*, 2006, **106**, 1105–1136.
23 M. Bühl and A. Hirsch, Spherical aromaticity of fullerenes, *Chem. Rev.*, 2001, **101**, 1153–1183.
24 H. D. Almeida Gonzalez, *et al.*, The Promise of Carbon Nano-Onions: Preparation, Characterization, and Their Application in Electrochemical Sensing, *Analysis Sensing*, 2025, **5**, e202400035.
25 B. T. Flinn, *et al.*, Sensing the Spin State of Room-Temperature Switchable Cyanometallate Frameworks with Nitrogen-Vacancy Centers in Nanodiamonds, *ACS Nano*, 2024, **18**, 7148–7160.
26 H. Liu, *et al.*, A review of carbon dots in synthesis strategy, *Coord. Chem. Rev.*, 2024, **498**, 215468.
27 S. Li, *et al.*, The development of carbon dots: From the perspective of materials chemistry, *Mater. Today*, 2021, **51**, 188–207.
28 S. Tao, T. Feng, C. Zheng, S. Zhu and B. Yang, Carbonized Polymer Dots: A Brand New Perspective to Recognize Luminescent Carbon-Based Nanomaterials, *J. Phys. Chem. Lett.*, 2019, **10**, 5182–5188.
29 M. Cutroneo, *et al.*, Polyvinylalcohol Composite Filled with Carbon Dots Produced by Laser Ablation in Liquids, *Polymers*, 2024, **16**, 1390.
30 L. Torrisi, L. Silipigni, A. Torrisi and M. Cutroneo, Luminescence in laser-generated functionalized carbon dots, *Opt. Laser Technol.*, 2024, **177**, 111089.
31 P. Bhatt, D. Kukkar, A. K. Yadav and K. H. Kim, Carbon dot-copper nanocomposite-based fluorescent sensor for detection of creatinine in urine samples of CKD patients, *Spectrochim. Acta, Part A*, 2024, **307**, 123666.
32 C. Ren, *et al.*, The fluorescence properties of nitrogen-doped carbon dots by microwave green approaches, *J. Mol. Struct.*, 2025, **1319**, 139364.
33 I. Kaur, *et al.*, Chemical- and green-precursor-derived carbon dots for photocatalytic degradation of dyes, *iScience*, 2024, **27**, 108920, DOI: **10.1016/j.isci.2024.108920**.
34 L. A. Essa and R. K. Jamal, Studying the structural and optical properties of carbon quantum dots prepared by electrochemical method, *J. Opt.*, 2024, **53**, 1574–1580.
35 Y. Liu, *et al.*, Electrochemical and colorimetric dual-channel biosensor based on B and N co-doped carbon nanotubes, *Microchem. J.*, 2024, **197**, 109770.
36 Y. Zhang, *et al.*, Synthesis of oil-soluble carbon dots via pyrolysis and their diverse applications in doxycycline detection, fluorescent ink, and film, *Spectrochim. Acta, Part A*, 2024, **304**, 123406.
37 T. Watcharamongkol, P. Khaopueak, C. Seesuea and K. Wechakorn, Green hydrothermal synthesis of multifunctional carbon dots from cassava pulps for metal sensing, antioxidant, and mercury detoxification in plants, *Carbon Resour. Convers.*, 2024, **7**, 100206.
38 C. Li, N. Li, L. Yang, L. Liu and D. Zhang, Synthesis of fluorescent carbon dots by B/P doping and application for Co2+ and methylene blue detection, *Spectrochim. Acta, Part A*, 2024, **309**, 123824.
39 S. Aydin, A. Yilmaz and M. Yilmaz, Green Synthesis of Various Heteroatom-doped Carbon Quantum Dots from Urine, Whey, and Their Mixture: The Optimization of Synthesis and Potential Applications, *ChemistrySelect*, 2024, **9**, e202304930.
40 N. Xu, H. Huang, H. Ouyang and H. Wang, Preparation of the heterojunction catalyst N-doping carbon quantum dots/P25 and its visible light photocatalytic activity, *Sci. Rep.*, 2019, **9**, 9971.
41 J. Li, *et al.*, Highly N,P-doped carbon dots: Rational design, photoluminescence, and cellular imaging, *Microchim. Acta*, 2017, **184**, 2933–2940.
42 D. Gu, L. Hong, L. Zhang, H. Liu and S. Shang, Nitrogen and sulfur co-doped highly luminescent carbon dots for sensitive detection of Cd (II) ions and living cell imaging applications, *J. Photochem. Photobiol., B*, 2018, **186**, 144–151.
43 L. S. Li and L. Xu, Highly fluorescent N,S,P tri-doped carbon dots for Cl− detection and their assistance of TiO2 as the catalyst in the degradation of methylene blue, *J. Photochem. Photobiol., A*, 2020, **401**, 112772.
44 A. B. Bourlinos, *et al.*, Green and simple route toward boron doped carbon dots with significantly enhanced non-linear optical properties, *Carbon*, 2015, **83**, 173–179.
45 P. Chen, *et al.*, Study on the photocatalytic mechanism and detoxicity of gemfibrozil by a sunlight-driven TiO2/carbon dots photocatalyst: The significant roles of reactive oxygen species, *Appl. Catal., B*, 2017, **204**, 250–259.
46 Z. Zhang, *et al.*, A minireview on doped carbon dots for photocatalytic and electrocatalytic applications, *Nanoscale*, 2020, **12**, 13899–13906.
47 K.-K. Niu, *et al.*, Nitrogen-doped carbon dots as photocatalysts for organic synthesis: Effect of nitrogen content on catalytic activity, *Nano Res.*, 2024, **17**, 4825–4833.

 This journal is © The Royal Society of Chemistry 2025

Published on 04 Juli 2025. Downloaded on 18.02.26 12:30:05.

48 S. Bhattacharyya, *et al.*, Effect of nitrogen atom positioning on the trade-off between emissive and photocatalytic properties of carbon dots, *Nat. Commun.*, 2017, **8**, 1401.
49 H. Kolya and C. W. Kang, Toxicity of Metal Oxides, Dyes, and Dissolved Organic Matter in Water: Implications for the Environment and Human Health, *Toxics*, 2024, **12**, 111.
50 D. Khandelwal, I. Rana, V. Mishra, K. R. Ranjan and P. Singh, Unveiling the impact of dyes on aquatic ecosystems through zebrafish – A comprehensive review, *Environ. Res.*, 2024, **261**, 119684.
51 H. Kumari, *et al.*, A Review on Photocatalysis Used For Wastewater Treatment: Dye Degradation, *Water, Air, Soil Pollut.*, 2023, **234**, 349.
52 L. Azeez, A. Lateef and O. Olabode, An overview of biogenic metallic nanoparticles for water treatment and purification: the state of the art, *Water Sci. Technol.*, 2023, **88**, 851–873.
53 R. B. González-González, *et al.*, Decontamination of emerging pharmaceutical pollutants using carbon-dots as robust materials, *J. Hazard. Mater.*, 2022, **423**, 127145.
54 C. Van Duijn, Toxic and photodynamic effects of toluidine blue on living bull spermatoza, *Exp. Cell Res.*, 1962, **26**, 373–381.
55 P. G. Kruger, B. Diamant and L. Scholander, Non-degranulating structural changes of rat mast cells induced by antigen and toluidine blue, *Exp. Cell Res.*, 1970, **63**, 101–109.
56 S. Qu, X. Wang, Q. Lu, X. Liu and L. Wang, A Biocompatible Fluorescent Ink Based on Water-Soluble Luminescent Carbon Nanodots, *Angew. Chem.*, 2012, **124**, 12381–12384.
57 Z. Yang, Y. Sun and F. Ma, Interlayer spacing of multilayer graphene oxide: Influences of oxygen-containing group density, thickness, temperature, and strain, *Appl. Surf. Sci.*, 2020, **529**, 147075.
58 R. S. Rajaura, *et al.*, Role of interlayer spacing and functional group on the hydrogen storage properties of graphene oxide and reduced graphene oxide, *Int. J. Hydrogen Energy*, 2016, **41**, 9454–9461.
59 L. C. Qin, D. Zhou, A. R. Krauss and D. M. Gruen, TEM characterization of nanodiamond thin films, *Nanostruct. Mater.*, 1998, **10**, 649–660.
60 J. A. Hammons, *et al.*, Submicrosecond Aggregation during Detonation Synthesis of Nanodiamond, *J. Phys. Chem. Lett.*, 2021, **12**, 5286–5293.
61 H. Li, *et al.*, Microwave-assisted synthesis of N,P-doped carbon dots for fluorescent cell imaging, *Microchim. Acta*, 2016, **183**, 821–826.
62 X. Miao, *et al.*, Synthesis of Carbon Dots with Multiple Color Emission by Controlled Graphitization and Surface Functionalization, *Adv. Mater.*, 2018, **30**, 1704740.
63 K. G. Nguyen, *et al.*, Investigating the effect of N-doping on carbon quantum dots structure, optical properties and metal ion screening, *Sci. Rep.*, 2022, **12**, 13806.
64 C. Wang, *et al.*, Biocompatible sulfur nitrogen co-doped carbon quantum dots for highly sensitive and selective detection of dopamine, *Colloids Surf., B*, 2021, **205**, 111874.
65 P. Ni, *et al.*, Optical properties of nitrogen and sulfur co-doped carbon dots and their applicability as fluorescent probes for living cell imaging, *Appl. Surf. Sci.*, 2019, **494**, 377–383.
66 S. R. Kamali, C. N. Chen, D. C. Agrawal and T. H. Wei, Sulfur-doped carbon dots synthesis under microwave irradiation as turn-off fluorescent sensor for Cr(III), *J. Anal. Sci. Technol.*, 2021, **12**, 48.
67 B. Zheng, *et al.*, One pot selective synthesis of water and organic soluble carbon dots with green fluorescence emission, *RSC Adv.*, 2015, **5**, 11667–11675.
68 Z. Ji, Z. Yin, Z. Jia and J. Wei, Carbon Nanodots Derived from Urea and Citric Acid in Living Cells: Cellular Uptake and Antioxidation Effect, *Langmuir*, 2020, **36**, 8632–8640.
69 M. L. Liu, B. B. Chen, C. M. Li and C. Z. Huang, Carbon dots: Synthesis, formation mechanism, fluorescence origin and sensing applications, *Green Chem.*, 2019, **21**, 449–471.
70 Reference Air Mass 1.5 Spectra, **https://www.nrel.gov/grid/solar-resource/spectra-am1.5.html**.
71 Z. Zhu, *et al.*, Synthesis of carbon dots with high photocatalytic reactivity by tailoring heteroatom doping, *J. Colloid Interface Sci.*, 2022, **605**, 330–341.
72 P. Innocenzi and L. Stagi, Carbon dots as oxidant-antioxidant nanomaterials, understanding the structure-properties relationship, A critical review, *Nano Today*, 2023, **50**, 101837.
73 N. Assad, A. Abbas, M. Fayyaz ur Rehman and M. Naeem-Ul-Hassan, Photo-catalytic and biological applications of phyto-functionalized zinc oxide nanoparticles synthesized using a polar extract of Equisetum diffusum D, *RSC Adv.*, 2024, **14**, 22344–22358.
74 L. Shen, *et al.*, One-Step Hydrothermal Synthesis of Sulfur Quantum Dots for Photoelectrochemical Catalysis for Dye Degradation, *J. Electron. Mater.*, 2022, **51**, 3092–3100.
75 Y. B. Li and F. X. Xiao, Surmounting the instability of atomically precise metal nanoclusters towards boosted photoredox organic transformation, *Chem. Sci.*, 2024, **16**, 2661–2672.
76 X. Yan, J. H. Dong, J. Y. Zheng, Y. Wu and F. X. Xiao, Customizing precise, tunable, and universal cascade charge transfer chains towards versatile photoredox catalysis, *Chem. Sci.*, 2024, **15**, 2898–2913.
77 X. Yan, H. Xie, G. Wu and F.-X. Xiao, Boosted solar water oxidation steered by atomically precise alloy nanocluster, *Chin. Chem. Lett.*, 2024, **36**, 110279.
78 D. Saini, *et al.*, Visible-Light-Promoted Photocatalytic Applications of Carbon Dots: A Review, *ACS Appl. Nano Mater.*, 2022, **5**, 3087–3109.
79 J. Brahmi, *et al.*, X-ray molecular structure characterization of a hexamethylenetetramine zinc(II) porphyrin complex, catalytic degradation of toluidine blue dye, experimental and statistical studies of adsorption isotherms, *J. Mol. Liq.*, 2021, **341**, 117394.
80 J. Z. Bloh, A holistic approach to model the kinetics of photocatalytic reactions, *Front. Chem.*, 2019, **7**, 128.

Published on 04 Juli 2025. Downloaded on 18.02.26 12:30:05.

81 D. Zhang, S. Lv and Z. Luo, A study on the photocatalytic degradation performance of a [KNbO3]0.9-[BaNi0.5Nb0.5O3-:δ]0.1 perovskite, *RSC Adv.*, 2020, **10**, 1275–1280.
82 W. F. Yao, *et al.*, Photocatalytic property of perovskite bismuth titanate, *Appl. Catal., B*, 2004, **52**, 109–116.
83 U. A. Rani, *et al.*, Sustainable production of nitrogen-doped carbon quantum dots for photocatalytic degradation of methylene blue and malachite green, *J. Water Process Eng.*, 2021, **40**, 101816.
84 N. Neelakandeswari, G. Sangami, N. Dharmaraj, N. K. Taek and H. Y. Kim, Spectroscopic investigations on the photodegradation of toluidine blue dye using cadmium sulphide nanoparticles prepared by a novel method, *Spectrochim. Acta, Part A*, 2011, **78**, 1592–1598.
85 Z. Guo, *et al.*, Designing nitrogen and phosphorus co-doped graphene quantum dots/g-C3N4 heterojunction composites to enhance visible and ultraviolet photocatalytic activity, *Appl. Surf. Sci.*, 2021, **548**, 149211.
86 U. Abd Rani, L. Y. Ng, C. Y. Ng, E. Mahmoudi and N. H. H. Hairom, Photocatalytic degradation of crystal violet dye using sulphur-doped carbon quantum dots, *Mater. Today: Proc.*, 2021, **46**, 1934–1939.
87 T. Selvakumar, *et al.*, Highly Efficient Sulfur and Nitrogen Codoped Graphene Quantum Dots as a Metal-Free Green Photocatalyst for Photocatalysis and Fluorescent Ink Applications, *ACS Omega*, 2022, **7**, 12825–12834.
88 Z. Qu, *et al.*, Carbon quantum dots/KNbO3 hybrid composites with enhanced visible-light driven photocatalytic activity toward dye waste-water degradation and hydrogen production, *Mol. Catal.*, 2018, **445**, 1–11.
89 A. B. Siddique, *et al.*, Synthesis of hydroxyethylcellulose phthalate-modified silver nanoparticles and their multifunctional applications as an efficient antibacterial, photocatalytic and mercury-selective sensing agent, *Int. J. Biol. Macromol.*, 2024, **256**, 128009.
90 A. B. Siddique, *et al.*, Thermodynamic and kinetic insights into azo dyes photocatalytic degradation on biogenically synthesized ZnO nanoparticles and their antibacterial potential, *Heliyon*, 2024, **10**, e40679.
91 S. O. Adewuyi, D. Malomo, S. M. Nelana, M. J. Klink and O. S. Ayanda, Kinetic Study of the Photocatalytic Degradation of Atrazine Over Copper Oxide Nanoparticles, *Water Conserv. Manag.*, 2024, **8**, 274–283.

 This journal is © The Royal Society of Chemistry 2025